ELSEVIER

Computer Physics Communications 89 (1995) 149–168

Computer Physics Communications

A piecewise parabolic method for cosmological hydrodynamics

Greg L. Bryan [a], Michael L. Norman [a], James M. Stone [b], Renyue Cen [c], Jeremiah P. Ostriker [c]

[a] *National Center for Supercomputing Applications, 5600 Beckman Institute, Drawer 25, University of Illinois at Urbana-Champaign, 405 North Mathews Avenue, Urbana, IL 61801, USA*

[b] *Department of Astronomy, University of Maryland, College Park, MD 20742, USA*

[c] *Princeton University Observatory, Princeton, NJ 08544, USA*

Abstract

We describe a hybrid scheme for cosmological simulations that incorporates a Lagrangean particle-mesh (PM) algorithm to follow the collisionless matter with the higher order accurate piecewise parabolic method (PPM) to solve the equations of gas dynamics. Both components interact through the gravitational potential, which requires the solution of Poisson's equation, here done by Fourier transforms. Due to the vast range of conditions that occur in cosmological flows (pressure differences of up to fourteen orders of magnitude), a number of additions and modifications to PPM were required to produce accurate results. These are described, as are a suite of cosmological tests.

1. Introduction

The standard view of the universe tells us that there are two kinds of matter: a baryonic component which makes up about 5% of the mass required to stop the universe from expanding forever, and a collisionless dark matter that appears to dominate the gravitational evolution of the universe and many of its components. Because the dark matter controls the dynamical evolution of the largest structures ($r \geq 5$ Mpc), and because the physics of the gaseous component is intrinsically much more complex, much effort has been focused on this component [6,7]. Unfortunately, we cannot directly observe dark matter and thus have, until recently, depended on the assumption that 'light follows mass' (i.e. that the baryonic component will generally follow the distribution of dark matter). This is known to be incorrect on scales up to cluster sizes (see, e.g., [1–3]) indicating a need to include the more difficult baryonic physics.

The physics of collisionless systems has led naturally to the development of particle based methods [4], while much success has been achieved in gas dynamics through the use of Eulerian techniques. Therefore, we combine a momentum conserving particle-mesh (PM) scheme for the collisionless component with the Godunov-based piecewise parabolic method (PPM) [5] for the gas. We have taken pains to use a state-of-the-art gas dynamics algorithm because of the demands of hydrodynamic cosmology. Temperatures can range over eight orders of magnitude, densities over six orders (neglecting the structure within galaxies) and pressures over 14 orders of magnitude. Even worse, many length scales are operating simultaneously: the ratio of the separation between clusters to the size of a cluster is about 100, requiring a minimum of 10^6 resolution

Elsevier Science B.V.
SSDI 0010-4655(94)00191-X

elements in three dimensions. PPM is one of the most effective of the shock capturing methods that have been developed recently [17]; it is formally third order accurate in space, easy to parallelize and quite robust in modelling cosmological flows. Even so, the unusual rigors of the cosmological simulation regime require certain modifications to the basic scheme. We also describe the changes necessary to make the PPM scheme function under limits of low resolution. This is extremely important due to the spectrum of length scales that are active in cosmological simulations. Short wavelength fluctuations are modulated by longer ones so both need to be treated as accurately as possible. Therefore we must insure that cosmologically interesting phenomena can be modelled with as small a number of zones as possible. To document and test the algorithms we have also developed a suite of cosmological test problems, the results of which are detailed.

Other approaches to numerical cosmology have been taken. Almost all use particle formulations of one sort or another for the dark matter, but they divide into two classes for the hydrodynamics: Lagrangean particle methods such as smooth particle hydrodynamics (SPH) and the Eulerian, hybrid methods. Examples of the former are [9,10] and the later codes are typified by [11,12].

There are still many physical processes that we have not included: the ionization state of the gas (due both to radiation and collisions), as well as radiative processes and radiative transfer effects. We will describe our efforts to implement the first two in a future paper, however the self-consistent inclusion of radiative transfer in such codes must await improved algorithms and better computers. Finally, we remark that magnetic fields and heat conduction are likely to play a role in cluster formation (and surely must be important in galaxy formation); however, their effects have not been examined here.

In Section 2, we describe the numerical methods used, with only a cursory description of PM and PPM, as they have both been described in adequate detail elsewhere. The cosmological test suite is presented in Section 3 and our conclusions are drawn in Section 4.

2. Numerical methodology

The first ingredient is to implement a particle-in-cell algorithm to trace the evolution of the dark matter. Such systems have been in use for many years and are well understood and well tested; for a fine description of their application to cosmology, see [6,7]. To be explicit, we implement a particle-mesh, cloud-in-cell [4] method with a grid size equal to the hydrodynamic mesh to facilitate the gravitational interaction. The computation of the gravitational potential is done by Fourier transform. We start therefore, with a description of the hydrodynamic algorithm.

We must solve the equations of ideal gas dynamics in a coordinate system that is comoving with the expanding universe (c.f. [13]):

$$\frac{\partial \rho_b}{\partial t} + \frac{1}{a}\vec{v}_b \cdot \nabla \rho_b = -\frac{1}{a}\rho_b \nabla \cdot \vec{v}_b, \tag{1}$$

$$\frac{\partial \vec{v}_b}{\partial t} + \frac{1}{a}(\vec{v}_b \cdot \nabla)\vec{v}_b = -\frac{\dot{a}}{a}\vec{v}_b - \frac{1}{a\rho_b}\nabla p - \frac{1}{a}\nabla \phi, \tag{2}$$

$$\frac{\partial E}{\partial t} + \frac{1}{a}\vec{v}_b \cdot \nabla E = -\frac{\dot{a}}{a}\left(3\frac{p}{\rho_b} + \vec{v}_b^2\right) - \frac{1}{a\rho_b}\nabla \cdot (p\vec{v}_b) - \frac{1}{a}\vec{v}_b \cdot \nabla \phi. \tag{3}$$

We use the proper peculiar baryonic velocity $\vec{v}_b \equiv a(t)d\vec{x}/dt$, proper pressure p, and modified gravitational potential ϕ which is related to the potential in proper coordinates Φ by

$$\phi \equiv \Phi + \frac{1}{2}a\ddot{a}\vec{x}^2.$$

The density, however, is comoving:

$\rho_b \equiv \rho_{b,proper}/a(t)^3$.

The expansion parameter $a \equiv 1/(1+z)$ follows the expansion of a smooth, homogeneous background, where z, the redshift, is a function only of t. All derivatives are determined with respect to the comoving position $\vec{x}$, which is defined simply to remove universal expansion from the coordinate system: $\vec{x} \equiv \vec{r}/a(t)$. The total fluid energy per unit mass (i.e. the specific energy) is E. The first equation represents the conservation of mass, the second, conservation of momentum, and the third, conservation of total fluid (kinetic plus thermal) energy. They are respectively, the first, second and third moments of the Boltzman equation. We actively solve the equation of total energy because of the need to enforce local energy conservation in any shock capturing scheme.

These equations are closed with the equation of state, the comoving form of Poisson's equation and by the formula for the expansion of an isotropic, homogeneous universe, which governs the evolution of the comoving coordinates:

$$E = p/\left[(\gamma - 1)\,\rho_b\right] + \vec{v}^2/2, \tag{4}$$

$$\nabla^2\phi = \frac{4\pi G}{a}(\rho_b + \rho_{dm} - \rho_0), \tag{5}$$

$$\frac{\ddot{a}}{a} = -\frac{4\pi G}{3a^3}(\rho_0 + 3p_0/c^2) + \Lambda/3. \tag{6}$$

Here, the densities are of the baryonic matter (ρ_b), the dark matter (ρ_{dm}) and the background (ρ_0), while p_0 is the background pressure, γ is the ratio of specific heats, and Λ is the cosmological constant. This system of equations is limited to the non-relativistic regime and assumes that curvature effects are not important – both assumptions are reasonable as long as the size of the simulated region is small compared to the radius of curvature and the Hubble length c/H (c is the speed of light and H is the Hubble constant).

The particles are governed by Newton's equations in comoving coordinates:

$$\frac{d\vec{x}_{dm}}{dt} = \frac{1}{a}\vec{v}_{dm}, \tag{7}$$

$$\frac{d\vec{v}_{dm}}{dt} = -\frac{\dot{a}}{a}\vec{v}_{dm} - \frac{1}{a}\nabla\phi. \tag{8}$$

The subscript 'dm' refers to dark matter particles.

An outline for the solution of these equations as well as the associated machinery that any simulation code must supply is given in Fig. 1. We will return to this figure in Section 2.7, after describing, in some detail, the action of each step.

2.1. Structure of the cosmological equations of hydrodynamics

We can examine the structure of Eqs. (1)–(3) to obtain a better understanding of the effect of each term. The derivatives are first order in time and provide us with the dependent variables that will be evaluated each time step: ρ_b, $\vec{v}$, and E.

The second term on the left hand side of each relation is due to our choice of Eulerian coordinates and corresponds to advection, the flow of conserved quantities (ρ_b, $\rho_b\vec{v}$, and $\rho_b E$) across the mesh. These will be termed the transport terms.

The first term on the right hand side of Eqs. (2) and (3) comes from our choice of comoving coordinates (a similar term also appears in Eq. (8), the velocity relation for the dark matter particles). It does not appear in the mass conservation Eq. (1) because of the comoving density definition. We note that these expansion terms could be eliminated entirely by the proper choice of variables (including time), although we have not done so here, as they do not constitute a major source of error.

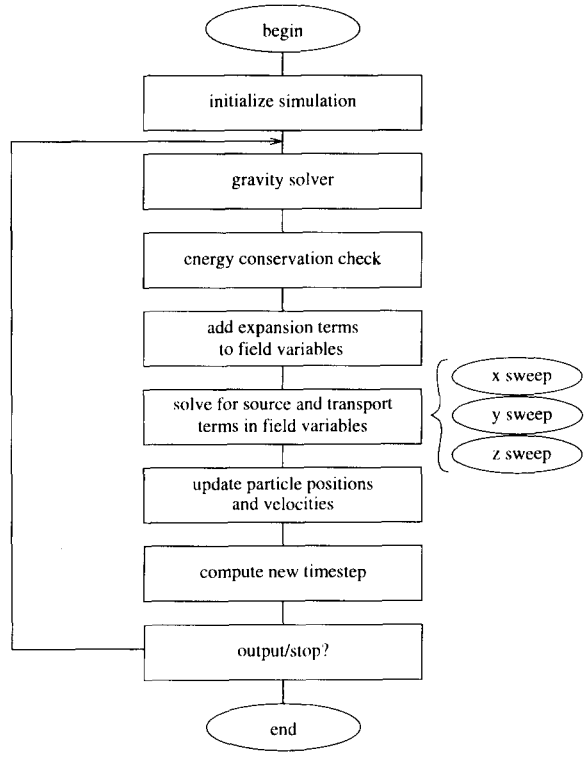

Fig. 1. Overview of KRONOS operations.

The remainder of the terms (due to pressure and gravity) are denoted as source terms. They drive instabilities and discontinuities in the flow. We make these distinctions because each of the three groups of terms have different numerical behaviour and are therefore treated differently. The source and transport steps will be solved in a self-consistent fashion by the PPM scheme while the expansion terms, which are spatially localized, are split off and solved in a separate step (as would be radiative cooling and heating, if present). This operator splitting has the effect of introducing a constraint on the time step by requiring that the coefficient $\dot{a}/a$ be small. Specifically, we insist that the expansion factor increase slowly,

$$\frac{\Delta a}{a} \leq C_a, \tag{9}$$

where Δa is the change in the expansion factor a per time step and C_a is a safety factor, which must be less than one for stability. To insure comparable accuracy with the rest of the scheme, we use $C_a = 0.01$. In practice, the time step constraint implied by this restriction is only important near the beginning of a simulation when the gas and dark matter are cold and fluctuations are small. At later times, as we shall see, other constraints place tighter limits on the time step.

The remainder of the terms (transport and source) in the fluid equations involve derivatives. Because we are interested in phenomena with no special geometry, we will restrict discussion to Cartesian coordinates. Once again we use the concept of operator splitting, but now apply it spatially. Here also, we split off the transport terms, writing the one-dimensional Lagrangean versions of Eqs. (1)–(3) as:

$$\frac{\partial}{\partial t}\frac{1}{\rho_b} = \frac{1}{a\rho_b}\frac{\partial v_b}{\partial x}, \tag{10}$$

$$\frac{\partial v_b}{\partial t} = -\frac{1}{a\rho_b}\frac{\partial p}{\partial x} - \frac{1}{a}\frac{\partial \phi}{\partial x}, \tag{11}$$

$$\frac{\partial E}{\partial t} = -\frac{1}{a\rho_b}\frac{\partial (pv_b)}{\partial x} - \frac{v_b}{a}\frac{\partial \phi}{\partial x}. \tag{12}$$

Now, x and v refer to the one-dimensional comoving position and peculiar velocity of the baryonic gas. These equations are now in a form that can be solved by the PPM scheme.

2.2. The piecewise parabolic method in cosmology

We now restrict ourselves to the solution of Eqs. (10)–(12), plus transport, in one dimension. This is accomplished by using a Lagrange plus remap scheme. There are two phases: first, solve the equations in Lagrangean form, and then remap the resulting distribution to Eulerian cells. This is described in detail in [5], but we will briefly outline the procedure in order to place the required changes in context. A schematic overview of the process is shown in Fig. 2. Additions required for a successful cosmological adaptation of the scheme are also shown and will be described in Sections 2.3–2.5.

The Lagrangean difference equations are:

$$\rho_j^{n+1} = \frac{a^n \rho_j^n \Delta x_j^n}{a^n \Delta x_j^n + \Delta t(\bar{v}_{j+1/2} - \bar{v}_{j-1/2})}, \tag{13}$$

$$v_j^{n+1} = v_j^n + \frac{\Delta t}{\Delta m_j}(\bar{p}_{j-1/2} - \bar{p}_{j+1/2}) + \Delta t(g_j^{n+1/2}), \tag{14}$$

$$E^{n+1} = E^n + \frac{\Delta t}{\Delta m_j}\left(\bar{v}_{j-1/2}\bar{p}_{j-1/2} - \bar{v}_{j+1/2}\bar{p}_{j+1/2}\right) + \frac{\Delta t}{2}\left(v_j^n + v_j^{n+1}\right) g_j^{n+1/2}. \tag{15}$$

We have used subscripts to indicate zone-centered (j) and face-centered ($j + 1/2$) quantities, while superscripts refer to position in time. The Lagrangean nature insures that the mass of an element $\Delta m_j = a^n \rho_j^n \Delta x_j^n$ does not change during the time step. Although they have been discretized in space, the accuracy of the update depends on how well we can compute the fluxes into and out of the cell during Δt. This in turn depends on our ability to compute the time-averaged (over Δt) values of p and v at the cell interfaces, denoted here by $\bar{p}_{j\pm1/2}$ and $\bar{v}_{j\pm1/2}$. We now describe the steps required to compute these quantities. Note that these difference equations (and the remap step that follows) are conservative.

We first construct monotonic piecewise parabolic (third order) interpolations in one dimension for each of ρ, v and p. The pressure is determined from Eq. (4), the equation of state. We have dropped the subscript b in this and the following two sections because we will be referring solely to baryonic quantities.

The interpolation formula for some quantity q (one of ρ, v and p) is given by

$$q(m) = q_{L,j} + x(\Delta q_j + q_{6,j}(1 - x)),$$
$$x \equiv \frac{m - m_{j-1/2}}{\Delta m_j}, \qquad m_{j-1/2} \le m \le m_{j+1/2}. \tag{16}$$

This is Eq. (1.4) of [5]. The mass coordinate m is the natural variable for interpolating in the Lagrangean step. The zones edges in the mass coordinates are $m_{j-1/2}$ and $m_{j+1/2}$ for the left and right edges, respectively. The quantities $q_{L,j}$, Δq_j, and $q_{6,j}$ can be viewed simply as interpolation constants; however, they also have more intuitive meanings. For example, $q_{L,j}$ is the value of q at the left edge of zone j, while Δq_j and $q_{6,j}$ are analogous to the slope and first order correction to the slope of q (see [5] for a complete discussion):

$$\Delta q_j \equiv q_{R,j} - q_{L,j}, \qquad q_{6,j} \equiv 6\left[q_j - 1/2\left(q_{L,j} + q_{R,j}\right)\right]. \tag{17}$$

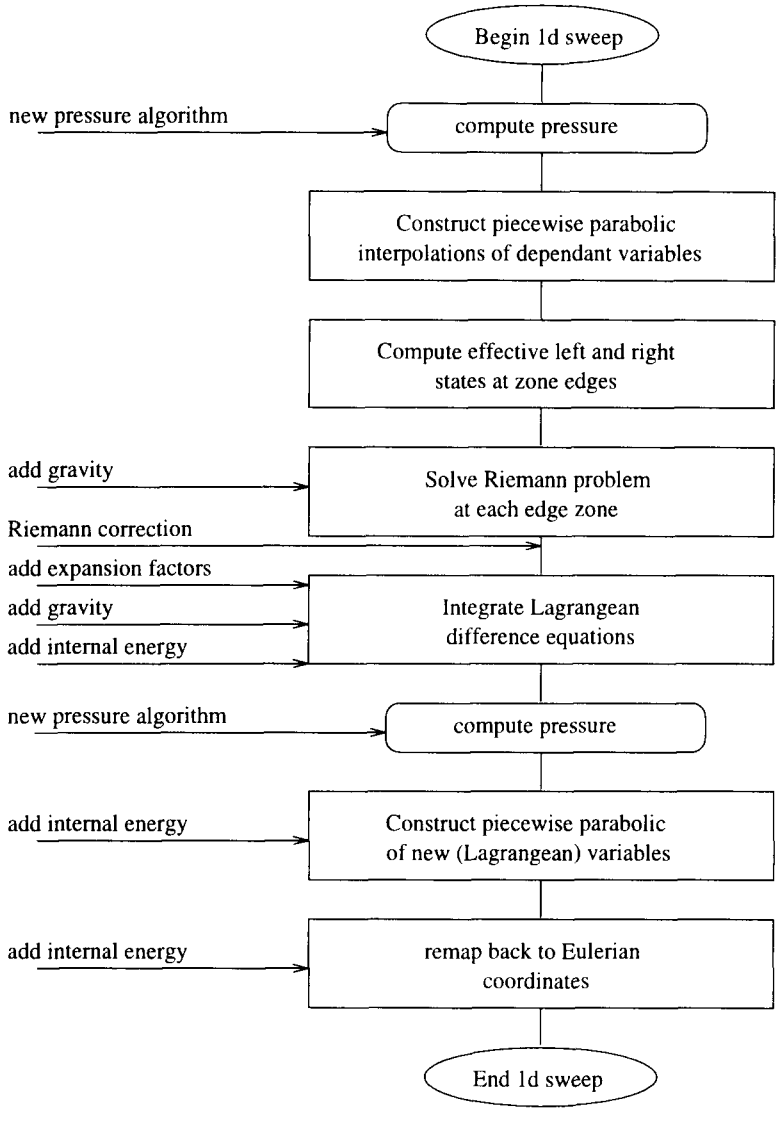

Fig. 2. Steps in a one-dimensional sweep to solve the fluid equations. Additions to the basic PPM scheme are labeled with arrows.

We have reduced the problem to finding $q_{L,j}$ and $q_{R,j}$. While this is simple in principle, it is complicated somewhat by the requirement that these values be of sufficient accuracy and that the resulting distribution be monotonic. That is, no new maxima or minima are introduced. The resulting formula are straightforward but complicated and are not reproduced here (but see Eqs. (1.7) to (1.10) of [5]).

Once we have the interpolation constants we compute the characteristic domain for each zone edge. This is simply the farthest a sound wave could travel in order to reach the interface by the end of a time step. The characteristic domain encompasses all of the information that can reach the zone edge during the current time step.

Here is the crux of the method: an average is taken over each of these domains to create, in effect, two constant states separated by a discontinuity. The advantage is that the solution to such a problem (called a Riemann problem) is well-known, self-similar and relatively easy to determine (although much work has gone

into approximations that are quick to compute). Its application insures that the Rankine-Hugoniot conditions are satisfied across a shock, thus avoiding the necessity of employing explicit artificial viscosity. It is implemented so that in the limit of smooth flow and no discontinuities, we solve the characteristic equations that produce time-centered quantities for p and v.

To determine the effective left and right states, we average over the domain of dependence on the appropriate side of the cell interface. This is given by

$$q^{+}_{j+1/2} = f_{j+1/2,L}(\Delta t C^{n}_{j}), \qquad q^{-}_{j+1/2} = f_{j+1/2,R}(\Delta t C^{n}_{j+1}), \tag{18}$$

where q^{+} (q^{-}) refers to the left (right) characteristic. Notice that we have approximated the characteristic sound speed as a constant within a cell. Here we use the Lagrangean sound speed $C^2 = \gamma p \rho$ rather than the Eulerian speed $c^2 = \gamma p/\rho$ because the interpolation is over mass. The functions f are just integrals over the parabolic interpolation formula:

$$f_{j+1/2,L}(y) = \frac{1}{y}\int_{m_{j+1/2}-y}^{m_{j+1/2}} a(m)\,dm, \qquad f_{j+1/2,R}(y) = \frac{1}{y}\int_{m_{j+1/2}}^{m_{j+1/2}+y} a(m)\,dm. \tag{19}$$

With these effective states, an approximation to the Riemann problem is found with an iterative approach (see [16]), producing estimates for $\bar{p}_{j\pm1/2}$ and $\bar{v}_{j\pm1/2}$ that are third order accurate in space and second order accurate in time.

After solving the difference Eqs. (13)–(15) for ρ^{n+1}, v^{n+1}, and E^{n+1}, we must remap these Lagrangean distributions to the original cells. The procedure is straightforward: construct piecewise parabolic interpolations (but now using E instead of p and including the transverse velocities v_y and v_z), and integrate over the distance each cell interface has moved. This is determined from $\bar{v}_{j+1/2}$.

2.3. Adding gravity to the PPM scheme

We need the time-centered gravitational acceleration $g^{n+1/2}$ for Eq. (15), computed here by finite differencing the potential $\phi^{n+1/2}$. If FFT's are used, a direct determination of the acceleration is possible (see [4]), but would require four transforms instead of two. This time-centered quantity should come from the advanced density distribution ($\rho^{n+1/2}$); however, that would render the scheme implicit. Therefore, we use a linear extrapolation from the previous two time steps:

$$\phi^{n+1/2} = \phi^{n}\left(1 + \frac{\Delta t^{n}}{2\Delta t^{n-1}}\right) - \phi^{n-1}\frac{\Delta t^{n}}{2\Delta t^{n-1}}. \tag{20}$$

Since the potential varies slowly, this is sufficiently accurate as long as the time step does not increase suddenly (a condition which we enforce, see below).

The acceleration required in Eq. (14) is actually the acceleration felt by the entire zone and not just at the zone center. Therefore, we find the mass weighted average acceleration over the zone by expanding the density and acceleration distributions and retaining all terms up to second order in Δx:

$$g^{n+1/2}_{j} = \frac{1}{2a^{n+1/2}\delta x_j}\left[\phi^{n+1/2}_{j+1} - \phi^{n+1/2}_{j-1} + \frac{1}{12}\left(\phi^{n+1/2}_{j+1} - 2\phi^{n+1/2}_{j} + \phi^{n+1/2}_{j-1}\right)\frac{\delta d_j}{d_j}\right]. \tag{21}$$

The success of the interpolation schemes in this method depends on the preservation of monotonicity. This must be done for the density slope δd_j, but not for the potential because it is only slowly varying,

$$\delta d_j = \min(|d_{j+1} - d_{j-1}|, 2|d^{n}_{j} - d^{n}_{j-1}|, 2|d^{n}_{j} - d^{n}_{j+1}|)\ \mathrm{sign}(d_{j+1} - d_{j-1})$$

$$\text{if } (d_{j+1} - d_j)(d_j - d_{j-1}) < 0, \tag{22}$$
$$= 0 \qquad \text{otherwise.}$$

This guarantees that the slope will not cause any interpolated value to exceed the density in the left or right zone, or, if the density at j is a local maxima or minima, it sets the slope to zero.

The other change required to adapt PPM for a body force is described in [5] and involves modifying the Riemann solver to account for gravity with the inclusion of a linear corrective term (not to be confused with the *post hoc* Riemann correction described in Section 2.5). This is relatively straightforward, although we note that a factor of one-half is missing from their Eq. (2.9): the factor Δt should read $\Delta t/2$.

2.4. The dual energy formulation for high Mach flows

The system described so far works well for gravitating systems with reasonable Mach numbers (< 100) as long as the structures are well resolved. This section and the next detail changes that are required to correctly account for situations in which one or both of these requirements are not met.

Large, hypersonic bulk flows appear to be very common in cosmological simulations and they present a problem because of the high ratio of kinetic energy E_k to gas internal energy e, which can reach as high as 10^8. Inverted, we see that the internal energy consists of an extremely small portion of the total energy. The pressure then, proportional to $E - E_k$, is the small difference between two large numbers: a disastrous numerical situation. This is not as large a problem as it may at first appear because it only occurs when the pressure is negligibly small. Therefore, even if we suffer large errors in the pressure distribution in these regions, the dynamics and total energy budget of the flow will remain unaffected. Nevertheless, if the temperature distribution is required for other reasons (e.g. radiative processes), a remedy is required.

To overcome this, we also solve the internal energy equation:

$$\frac{\partial e}{\partial t} + \frac{1}{a}\vec{v}\cdot\nabla e = -\frac{3(\gamma-1)\dot{a}}{a}e - \frac{p}{a\rho}\nabla\cdot\vec{v} \tag{23}$$

in comoving co-ordinates. The structure is similar to the total energy equation; the second term on the left hand side represents transport, while the first term on the right is due to expansion of the coordinate system. These are treated as before. It is differenced (again, in Lagrangean form without the expansion term) as

$$e_j^{n+1} = e_j^n + \frac{\Delta t}{\Delta m_j} p_j^{n+1/2}(\overline{v}_{j-1/2} - \overline{v}_{j+1/2}). \tag{24}$$

The time-centering of the pressure in this equation is essential to avoid the accumulation of entropy errors, but we would still like to retain the explicit nature of algorithm. Therefore, we adopt $p_j^{n+1/2} = (\overline{p}_{j-1/2} + \overline{p}_{j+1/2})/2$.

It is necessary, however, to conserve the total energy so that the conversion of kinetic to thermal energy is performed properly. We must therefore, combine the two formulations without allowing the separately advected internal energy e to play a role in the gas dynamics. This is done by carrying both terms through the simulation and using the total energy E for hydrodynamic routines and the internal energy e when the temperature profile is required. One way to view this procedure is to treat e as enhanced precision (extra digits) for E that automatically 'floats' to where it is needed. We only require that they be kept synchronized when the two levels of precision overlap.

When the pressure is required solely for dynamic purposes, the selection criterion operates on a cell by cell basis using

$$p = \begin{cases} \rho(\gamma-1)(E - \vec{v}^2/2), & (E - \vec{v}^2/2)/E > \eta_1, \\ \rho(\gamma-1)e, & (E - \vec{v}^2/2)/E < \eta_1. \end{cases} \tag{25}$$

It should be stressed that as long as the parameter η_1 is small enough the dual energy method *will have no dynamical effect*. We use $\eta_1 = 10^{-3}$ which is consistent with the truncation error of the scheme. We are now free to select the method by which the internal energy field variable e is updated so that it will not become contaminated with errors advected by the total energy formulation but still give the correct distribution in shocked regions. Since we are concerned with the advection of errors, the selection criterion must look at each cell's local neighbourhood. In one dimension, this is done with

$$e = \begin{cases} (E - \vec{v}^2/2), & \rho(E - \vec{v}^2/2)/\max(\rho_{j-1}E_{j-1}, \rho_j E_j, \rho_{j+1}E_{j+1}) > \eta_2, \\ e, & \rho(E - \vec{v}^2/2)/\max(\rho_{j-1}E_{j-1}, \rho_j E_j, \rho_{j+1}E_{j+1}) < \eta_2. \end{cases} \tag{26}$$

Thus, η_2 determines when the synchronization (of e with E) occurs. Too high a value may mask relatively weak shocks, while spurious heating (via contamination) may occur if it is set too low. After some experimentation, we have chosen $\eta_2 = 0.1$, a somewhat conservative value.

We note that others have independently developed a similar but distinct scheme for dealing with this problem, which is endemic to methods adopting the total energy equation. In Ref. [12] the two variables adopted are total energy and entropy (rather than total energy and thermal energy), with an analogous scheme for choosing which variable to employ.

2.5. *The correction to the Riemannn solver*

Body forces, such as gravity, are included in the Riemannn solver as a linear term [5]. This is sufficient as long as the structures being computed are resolved and we can clearly distinguish between gravity-induced pressure gradients and shock waves. Unfortunately, this is not always possible in gravitational clustering. The problem manifests itself in the early stages of an object's collapse, when it is contained within two zones (the resolution element for most shock capturing codes). Here, the scheme underestimates the time averaged pressure ($\overline{p}_{j+1/2}$) between the zones. This is a consequence both of the fact that the body force is only included to first order in the Riemann solver and the monotonicity constraints which tend to clip local peaks in the density and pressure distributions. We therefore apply a correction of the form

$$\overline{p}_{j+1/2} = \max\left[\overline{p}_{j+1/2}, (v_j - v_{j+1})\max(d_j, d_{j+1})\max(0, v_j - v_{j+1})\right]. \tag{27}$$

This largely *ad hoc* estimate converts the energy of motion between the two zones into thermal energy if they are colliding. This thermal energy is then used as a new estimate for the time-averaged pressure between zones only if it is larger than the estimate from solving the Riemann problem. To prevent its application outside of underresolved, collapsing regions, we also demand that a strong overdensity be present:

$$d_j/d_{j-1} > 2 \quad \text{and} \quad d_{j+1}/d_{j+2} > 2. \tag{28}$$

The factor of two in this constraint comes from applying the method to underresolved distributions with known solutions, such as the spherical collapse [18] and the Zel'dovich pancake [22,23] as well as self-convergence tests.

This correction must also be applied to $p_j^{n+1/2}$, the pressure used in the internal energy update. Here we are dealing with zone centers, so the correction becomes

$$p_j^{n+1/2} = \max\left[p_j^{n+1/2}, d_j^n(\overline{v}_{j-1/2} - \overline{v}_{j+1/2})\max(0, \overline{v}_{j-1/2} - \overline{v}_{j+1/2})\right], \tag{29}$$

again with the requirement of a (zone-centered) overdensity of factor two.

To maintain consistency with the dual energy formulation, we reset $p_j^{n+1/2}$ to $(\gamma - 1)e_j\rho_j$ if this cell used the total energy (26) to obtain its pressure.

2.6. The Layzer-Irvine cosmic energy equation

An important test of any numerical method is energy conservation. Following [13], we write the comoving equation of total (gravitational plus fluid) energy conservation (c.f. [14,15]) as

$$\frac{d}{dt}(K+U+W)+\frac{\dot{a}}{a}(2K+3P+W)=0. \tag{30}$$

The symbols K, U, and W refer to the average comoving kinetic, internal and potential energies, respectively and we have defined P to be the average com oving pressure.

The expression can be integrated over time and discretized to read

$$a^n(K^n+W^n+U^n)+\sum_{m=1}^{n}[K^{m-1/2}+(3\gamma-4)U^{m-1/2}]\Delta a^{m-1/2}=a^0(K^0+W^0+U^0). \tag{31}$$

In the limit of no expansion ($a=1$ and $\dot{a}=0$), we recover the usual conservation of total energy. We integrate this equation along with the dynamical equations to monitor energy conservation.

2.7. Code structure and overview.

We now return to the organizational structure of the code (Fig. 1). The first step must be to create or load the initial conditions. We use the Zel'dovich approximation to set up the particle distribution, as described in [6]. For a set of particles initially placed at grid centers, this produces displacement vectors and velocities for each of the particles. The baryonic density and velocity distribution is found as in [11].

Next we enter the main loop, calculating the potential using fast Fourier transform techniques [4], and then checking energy conservation for adiabatic simulations (Section 2.6). The expansion terms are updated and then the PPM scheme is used to solve for the hydrodynamic variables. Finally, the particle positions and velocities are updated with a time centered second order method.

The time step is chosen from the minimum of the expansion time step (9), the Courant condition and the requirement that a particle move no more than half a cell's length in a single time step.

The Courant condition is given by

$$\Delta t \leq \min\left\{\left[C_0 a(t)\,\Delta x\right] / \left[C_s+\max\left(|v_x|,|v_y|,|v_z|\right)\right]\right\}, \tag{32}$$

where C_s is the local sound speed, v_x, v_y, v_z are the local fluid velocities and C_0 is the Courant number, typically $C_0 \approx 0.5$. The minimum is over all cells. We also demand that the time step increase by no more than 25% from its previous value and add the requirement that the universe expand by no more than 2% in linear dimension within one time step.

The code uses dimensionless units. Specifically, length is in units of the box width, density is in units of the mean comoving density

$$\rho_0=\frac{3\Omega_0 H_0^2}{8\pi G}(1+z)^3,$$

and time is normalized by $1/\sqrt{4\pi G\rho_0}$, where H_0 is the Hubble constant at the current epoch.

3. Cosmological tests

The PPM method has been subjected to a number of pure hydrodynamic tests many of which are described in detail by [17]. It performs very well on tests involving strong shocks, common in astrophysical flows.

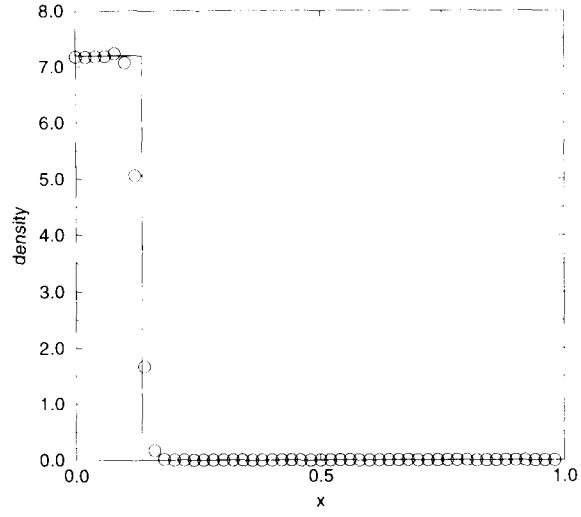

Fig. 3. The density distribution of the planar one-dimensional pressureless collapse at 0.927 free fall times. The analytic solution is denoted by a solid line.

Similarly particle-mesh codes have been extensively benchmarked [4,6]. We will therefore concentrate on tests that model physical situations which are expected to arise in cosmological simulations.

3.1. One-dimensional pressureless collapse

As a first test of the gravity solver and advection routines we model the two sided one-dimensional collapse of a homogeneous plane parallel cloud in Cartesian coordinates. This is similar to the gravitational collapse of a sphere in spherical coordinates [19] and an analytic solution describes the collapse of every mass layer,

$$(x/x_0) = 1 - 2\pi G\rho_0 t^2, \qquad (\rho/\rho_0) = (1 - 2\pi G\rho_0 t^2)^{-1}. \tag{33}$$

Here, the time for any mass layer to reach the origin (the free fall time) is $t_{ff} = \sqrt{1/(2\pi G\rho_0)}$. The initial density at $t = 0$ is ρ_0 and the fluid starts at rest. To make the run, we use units such that $\rho_0 = 1$ and $G = 1$, making $t_{ff} = 0.399$. Isolated boundary conditions are used as described in [21]. In Fig. 3, we show the density distribution at $t = 0.37$, considerably advanced in the evolution. For a numerical example of this problem in spherical coordinates, see [20]. Note that the universal expansion terms are not used in either this problem or the next (i.e. $a = 1$).

3.2. The Jeans instability

As a natural extension of the previous problem, we add pressure forces. This introduces a length scale but also produces a non-linear system of equations with no general analytic solution. However, by linearizing the equations around the homogeneous solution (pressure p_0 and density ρ_0) we obtain a solution with two cases: a travelling wave or a growing perturbation. The condition that differentiates these two situations is the familiar Jeans criterion, which we write as

$$p_c = \frac{G\rho_0^2\lambda^2}{\gamma\pi}, \tag{34}$$

where λ is the wavelength of the perturbation and p_c is the critical pressure. If the ambient pressure is above it, the wave oscillates and if it is below, the wave grows.

In order to determine the code's ability to discriminate between these two cases, we impose a perturbation wavelength of 64 zones and vary the pressure in small increments around the critical pressure. We find that the value given in Eq. (34) is reproduced to within $\Delta p/p_c = 0.01$.

3.3. Adabatic expansion

In order to test the time-integration accuracy of the expansion terms, we turn universal expansion on and adopt a completely homogeneous universe with initial temperature $T_i = 200$ K and $v_i = 100$ km/s at an initial redshift of $z_i = 20$. The expansion terms in Eqs. (1)–(3) operate like drag terms, so that in the absence of a source, the velocity decreases as $v = v_i a^{-1}$ and the temperature as $T = T_i a^{-2}$. Using $C_a = 0.01$, the computed temperature at $z = 0$ was $T_f = 0.2255$ K, 0.57 % below the analytic result of 0.2268 K. The final computed velocity was $v_f = 4.749$ km/s, compared to 4.762 km/s, a 0.27 % discrepancy.

3.4. The linear phase of the one-dimensional Zel'dovich pancake

This test (described in Sections 3.4 and 3.5) is particularly pertinent to cosmological studies not only because it encompasses all of the physics (hydrodynamics, expansion and self-gravity), but also because it represents an idealized, isolated caustic formation. One can think of the problem as a single-mode analysis of the full three-dimensional simulation. The initial conditions are relatively simple; we simply place a linear, sinusoidal perturbation in a one-dimensional box and follow its evolution. A solution to the equations (which can also be used to set up the initial state) for a flat cosmology is [22,23]

$$\begin{aligned} \rho(x_l) &= \rho_0 \left[1 - \frac{1+z_c}{1+z}\cos(kx_l)\right]^{-1}, \\ v(x_l) &= -H_0 \frac{1+z_c}{(1+z)^{1/2}} \frac{\sin(kx_l)}{k}, \\ T(x_l) &= T_{init} \left[\frac{\rho(x_l)}{\bar{\rho}}\right]^{2/3}. \end{aligned} \tag{35}$$

Here, z_c is a free parameter and is the redshift at which the Zel'dovich results 'pancake', or form caustics. H_0 is the current value of the Hubble constant, often parameterized as $H_0 = 100h$ Mpc/km/s, and $k = 2\pi/\lambda$ where λ is the perturbation wavelength. We note that this solution is exact in one dimension up until the point of caustic formation. However, these expressions are in terms of Lagrangean positions x_l, so we need to convert the Eulerian coordinates of the code (x_e) into Lagrangean coordinates:

$$x_l - \frac{1+z_c}{1+z_i}\frac{\sin(kx_l)}{k} = x_e. \tag{36}$$

As a check of the linear evolution, we set up a model from an initial redshift $z_i = 100$ with the following parameters: 256 zones, $T_{init} = 10^2 K$, $\lambda = 64h^{-1}$ Mpc, $h = 0.5$ and $z_c = 1$. Defining the L_1 error norm as

$$(\Delta\rho) = \frac{1}{N}\sum_{i=1}^{N}\left|\frac{\rho(x_l) - \rho_{numerical}}{\rho_0}\right|, \tag{37}$$

for density and adopting a similar definitions for v, we make the run with N, the number of grid points spanning the perturbation, ranging from 8 to 64. The errors should decrease as Δx^{-r} where r is the convergence rate.

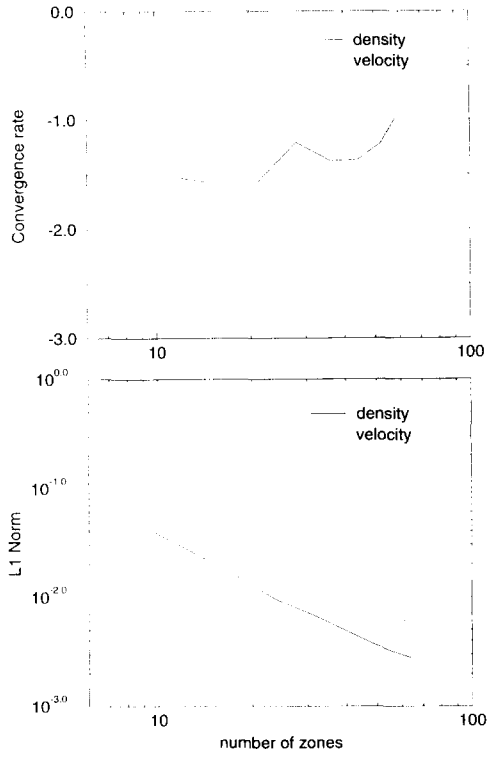

Fig. 4.

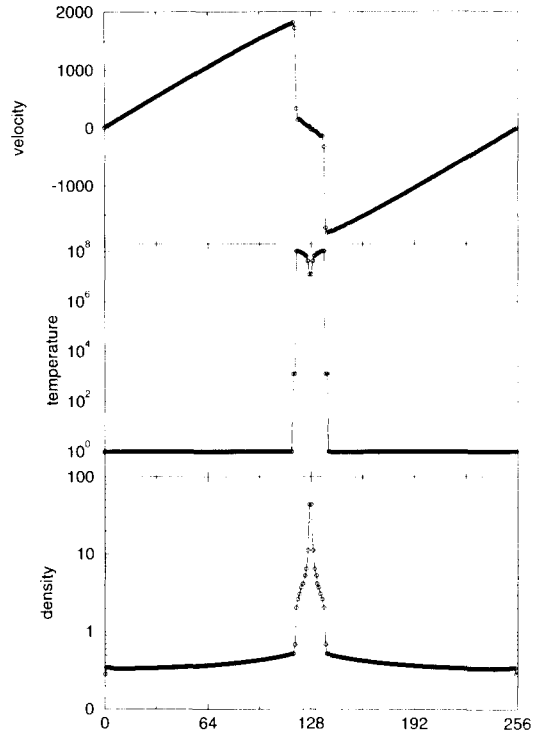

Fig. 5.

Fig. 4. Convergence rates and L1 error norms for the density and velocity fields in the one dimension Zel'dovich pancake.

Fig. 5. The velocity (top), temperature (middle) and density (bottom) for a one-dimensional Zel'dovich pancake at a redshift of $z = 0$. Velocity is in km/s, temperature in K, while the density is in units of the current background density required for a flat universe.

In Fig. 4, we plot both the error and the convergence rate, as found by computing the slope of the logarithmic derivative of the error with respective to N. We see that the velocity converges as $r \sim 2$ and the density as $r \sim 1.5$.

3.5. *The non-linear phase of the one-dimensional Zel'dovich pancake*

The non-linear phase of evolution for the caustic is of more practical interest in cosmology, as well as being more difficult than the linear evolution. Fig. 5 shows the solution at $z = 0$ (using the same initial conditions as in Section 3.4) at a resolution of 256 zones, demonstrating the strong shocks and large gradients involved. The shock is well delineated and the temperature profile of the very cold gas is still accurate (until it drops below 1 K which we have instituted as an artificial minimum).

We have also performed this test at a number of different resolutions in order to gauge the method's ability to resolve the evolution with a small number of zones. This characteristic is crucial because of the range of wavelengths active in hierarchical cosmological models. The results (at $z = 0$) using 8, 16 and 32 zones are shown in Fig. 6. Solid lines represent the solution computed at a much higher resolution (1024 zones) and then degraded to the appropriate scale. We do not show examples with more than 32 zones because they exhibit almost no difference from the converged solution (once it is binned to the lower resolution).

Clearly, even with eight zones the main features are right: a sharp central density peak causes a shock to

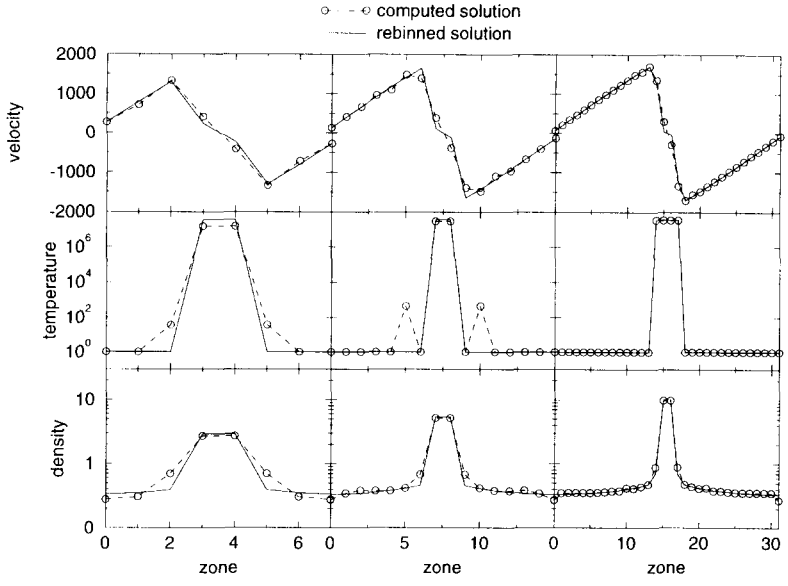

Fig. 6. The velocity (top), temperature (middle) and density (bottom) for a one-dimensional Zel'dovich pancake at a redshift of $z = 0$. Open circles with dotted lines depict the solution computed with 8,16 or 24 zones (left, center or right panels), while the solid lines represent the solution computed with 1024 zones and degraded to the appropriate number of zones. Units are as in the previous figure.

form and move outward from the central plane. The density distribution in each case is very close to its correct shape, although the zones next to the peak are slightly elevated (this is due to the monotonicity of the scheme and not to an explicit diffusion). The pressure and temperature in the central peak are somewhat below the high resolution results, especially for the eight zone test. This is unavoidable as the artificially widened peak (a minimum of two zones for the symmetric case considered here) puts a limit on how much potential energy can by converted to kinetic and thermal energy (see Fig. 8). There is some low temperature jitter (caused by the dual energy formulation), but the most important characteristics are the sharp shocks and low diffusion, even at poor resolution.

In order to gauge the self-convergence rate in the non-linear regime, we must redefine the error norm because the strong shock causes changes in some quantities by a factor of 10^8. We adopt, for a quantity q (one of T, v or ρ),

$$(\Delta q) = \frac{1}{N}\sum_{i=1}^{N} \frac{|q_i - q_{1024,i}|}{\max(|q_i|, |q_{1024,i}|)}, \tag{38}$$

where $q_{1024,i}$ is computed by linear interpolating between points in of a high resolution solution computed with 1024 cells. The effect of using the maximum of the two quantities in the denominator is to force each term in the error to be between zero and one. Fig. 7 shows the error for a number of different resolutions. Although the sharp shock causes some noise, the convergence rate appears to be $r \sim 1$. The presence of a discontinuity prevents a convergence rate better than one.

In Fig. 8, we show the dependence of the various energy terms on resolution, as well as the fractional energy gain or loss (defined as the ratio of the difference between the right and left hand sides of Eq. (31) to $a^n W^n$). The drop in thermal energy seen below 32 zones is due to the inability of the small mesh to represent such a narrow central peak. This makes the magnitude of the potential energy too small. The thermal energy mirrors this, but the kinetic energy remains constant and does not decline as it should. Once again, this is due to a

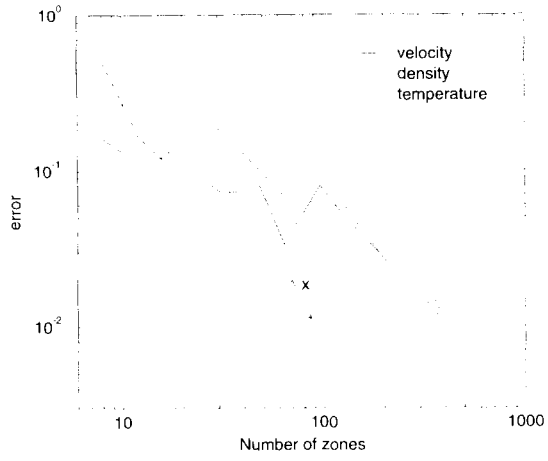

Fig. 7. The self-convergence error (see text for a definition) of the non-linear phase ($z = 0$) of the Zel'dovich pancake. The arrow shows a convergence rate of 1.

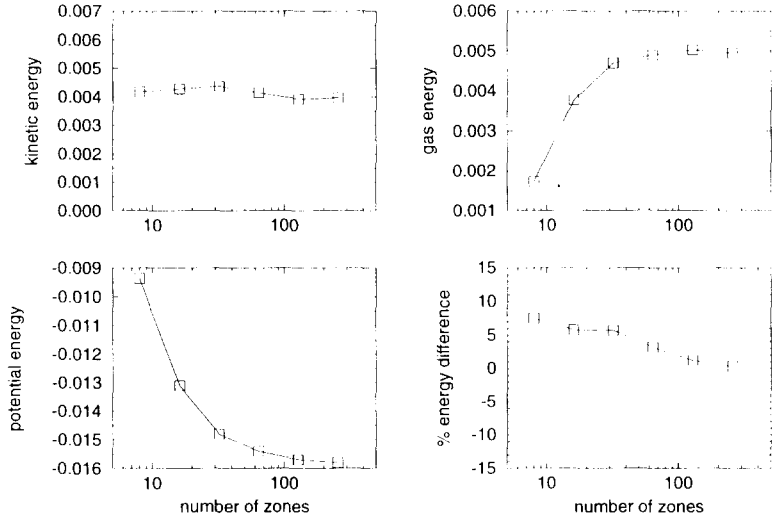

Fig. 8. The kinetic energy (top right), thermal energy (top left), gravitational potential energy (bottom left) and fractional energy gain or loss (bottom right) for the one-dimensional Zel'dovich pancake at various resolutions. All energies are in dimensionless units.

lack of resolution. Immediately after the peak is formed, it is two zones wide (due to the symmetry of the initial conditions), while the true distribution is much narrower. Insufficient thermal energy has been produced to support this artificially thick structure and it should collapse further but is prevented by the coarseness of the grid. One can think of this as a fictitious 'grid' force that is not represented in the energy equation and so shows up as a violation of energy conservation. It applies to highly under-sampled structures and represents only a small amount of energy compared to larger and better resolved wavelengths. We also point out that the problem is not specifically related to the scheme chosen and should be present in any grid based method that produces such narrow density distributions.

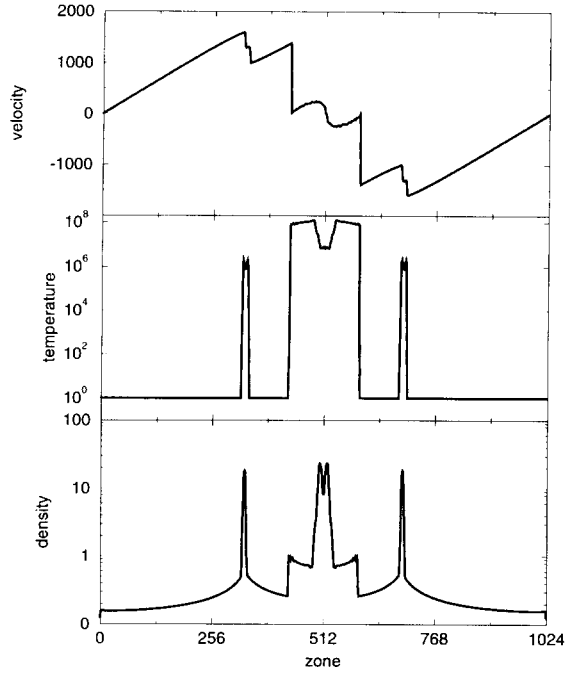

Fig. 9.

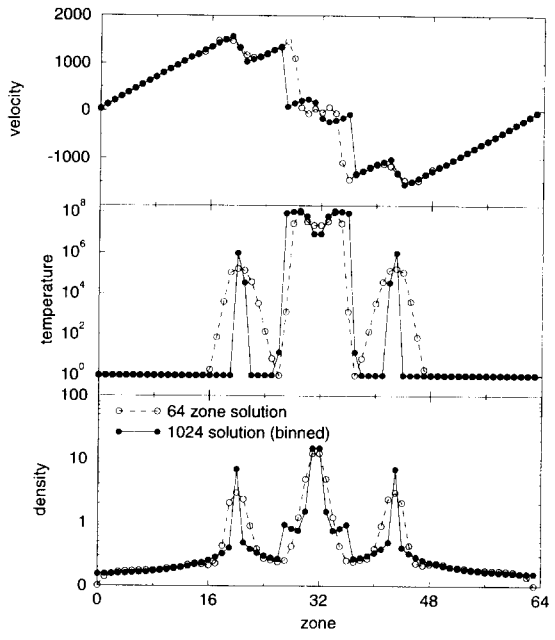

Fig. 10.

Fig. 9. The velocity (top), temperature (middle) and density (bottom) for a double one-dimensional Zel'dovich pancake at a redshift of $z = 0$. Units are as in the previous figures.

Fig. 10. The velocity (top), temperature (middle) and density (bottom) for a double one-dimensional Zel'dovich pancake at a redshift of $z = 0$. Open circles with dotted lines depict the solution computed with 64 zones, while the solid lines with filled circles represent the solution computed with 1024 cells and degraded to 64 zones. Units are as in the previous figure.

3.6. The double pancake with a strong and weak shock

In order to subject the dual energy formulation to a stringent test we have superimposed a smaller perturbation with one fourth of the wavelength onto the pancake described above. Using the same formulation as in the previous problem, we adopt $z_{c2} = 0.45$ and $\lambda_2 = 16h^{-1}$ Mpc. Note that z_c no longer refers to the redshift of peak formation (since the two perturbations interact) but is related to the amplitude of the imposed sinusoid. In Fig. 9, we show a high resolution computation at $z = 0$, by which time the two central peaks have nearly combined. The side peaks are present but at a much smaller amplitude because they are in the low density region created by the main collapse. The ratio of kinetic to thermal energy in the two smaller peaks is about 10^3, illustrating an occasion when the dual energy formalism is required.

Fig. 10 shows the results computed with 64 grid points and contrasted with the 1024 zone solution degraded to 64 zones. The strong central shocks on either side of high density plateau are well realized and near their correct locations. The smaller peaks have been stretched by the velocity field of the stronger, inner fluctuations making the profiles wider than in the high resolution run. The shocks are also much weaker, having been modulated by e, the internal energy formulation. Notice that while this produces wider, less clearly defined shocks, they are still reasonably accurate. The main features of the flow are present even though the thermal energy in the smaller shocks is one tenth of one percent of their energy of bulk motion and each wavelength is resolved by less than sixteen zones. These last two conditions make this a difficult test for any cosmological code.

3.7. Two-dimensional self-convergence tests

As a final test, we compute a two-dimensional cold dark matter universe in order to test the self-convergence in a more realistic, multi-dimensional test (the parameters are identical to those in the next section, except, of course, for being two-dimensional). Performing these tests in only two dimensions increases the dynamical range that can be obtained with only a modest expenditure of computational resources. We run the simulations at a variety of resolutions in order to investigate the self-convergence properties of the code. In order to do this, however, we must insure that the physical problem we are solving is the same at each resolution. Since the initial conditions contain a spectrum of length scales, we must introduce an artificial cutoff in the power spectrum of initial perturbations. This is done such that the shortest wavelength used for the initial conditions is the the Nyquist wavelength of the smallest box to be examined, here 64 zones on a side.

The results at the end of the simulation ($z = 0$) for 64^2, 128^2 and 256^2 grid points are shown in Fig. 11. Since the shortest perturbations are just two zones in the 64^2 box we do not expect such short wavelengths to be accurately evolved. Nonetheless, the correspondence between recognizable features in the three simulations is gratifying. It is clear from a visual inspection that the structures created are quite robust, despite the fact that they are often intrinsically much thinner than the grid can handle. Larger simulations have been computed, up to 1024^2, and no new features are observed, although the caustics continue to be thinner at higher resolution.

In order to be more quantitative, we have degraded the 1024^2 zone solution by averaging the density (and density weighted temperature) of all the high resolution cells that lie within a lower resolution zone. This gives a one-to-one correspondence between solutions computed with different resolutions. Scatter plots are presented for the 64^2 solution in Fig. 12 and 256^2 in Fig. 13. Our earlier statements are confirmed. Although the scatter is fairly large in the first figure, there is correspondence over four orders of magnitude in temperature and two orders in density. The second plot displays even better agreement between the lower and high resolution runs.

3.8. Comparison with other codes

We have also, with others, carried out a comparison of this method with other modern cosmological codes, both Eulerian and Lagrangean. In order to examine a realistic model with the effects of dark matter, we computed the evolution of a flat, pure baryon universe using initial conditions from the cold dark matter (CDM) scenario. Although this is not a viable model, it does present a clearly defined test problem that does not depend on the N-body solver. The method for producing initial conditions has been described elsewhere [24,11,6] and can be parameterized in terms of Ω, the ratio of the average density to that required to close the universe and σ_8, the amplitude of mass fluctuations in a sphere of radius 8 h^{-1} Mpc at $z = 0$. We choose the canonical values $\Omega = 1$, $\sigma_8 = 1$, $h = 0.5$ and used a physical box of length 64 h^{-1} Mpc. Four runs were performed, using grids of 32^3, 64^3, 128^3 and 256^3 with the same initial conditions smoothed to the Nyquist wavelength of the 64^3 cube. The simulations were run from $z_{init} = 20$ to $z = 0$.

The simulations are analyzed in detail in [25] and we will not repeat the analysis here, except to comment that the results only serve to strengthen our conclusion that this scheme is robust and accurate.

4. Conclusions

We have described the changes necessary for applying the third order accurate, shock capturing hydrodynamics scheme PPM to cosmological systems. The range of scales makes this a very difficult problem and has forced the adoption of an unusual method for dealing with the presence of weak shocks in supersonic flows. Although this method is not particularly elegant it does seem to produce the correct results. The correction to the Riemannn solver is also somewhat *ad hoc* and work is underway to incorporate self-gravity in a more self-consistent fashion.

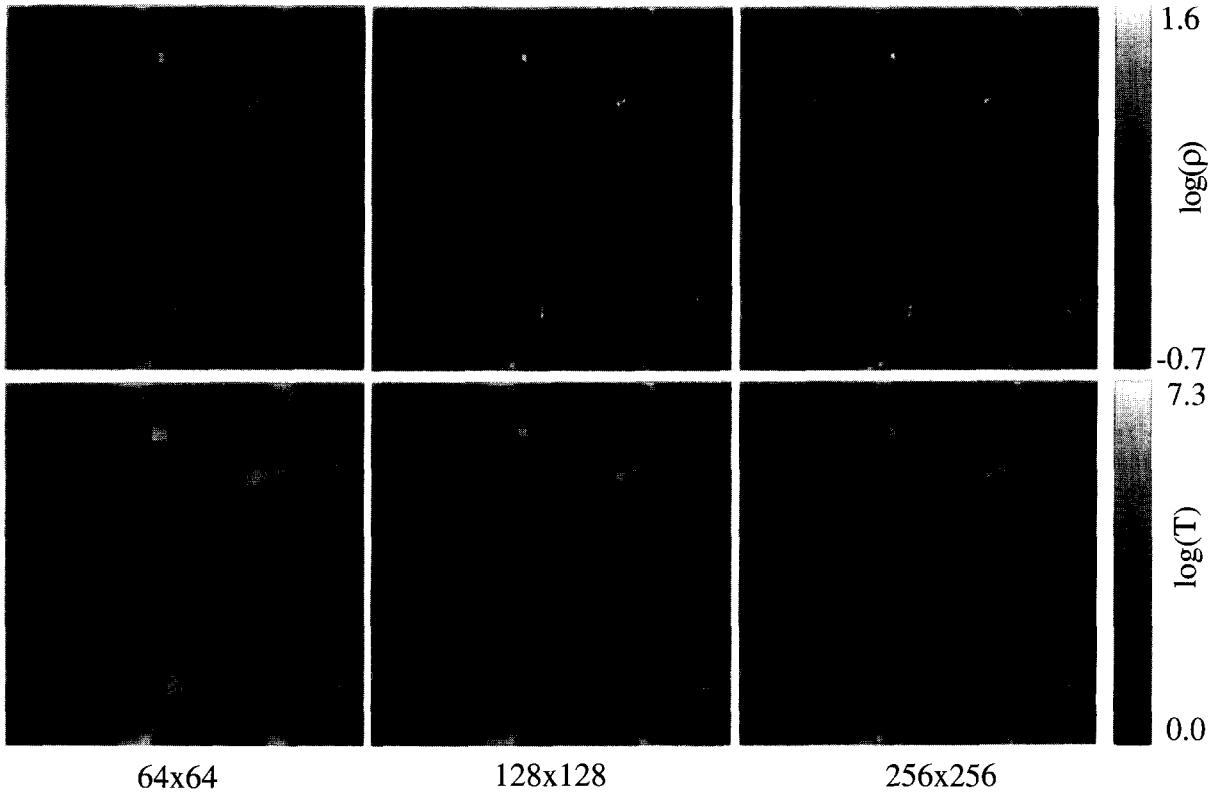

Fig. 11. Greyscale plots of the logarithm of density (top three panels) and temperature (bottom three panels) for a two-dimensional CDM simulation computed with the same initial conditions at three different resolutions: 64 × 64 (left panels), 128 × 128 (central panels) and 256 × 256 zones (right panels). Temperature is in degrees Kelvin, density in units of the present density required to close the universe.

We have also presented the results of a series of tests selected for their relevance to cosmological studies. The guiding philosophy in presenting this test suite is not only to show that the correct results are produced with sufficient resolution, but also to demonstrate that the solutions under conditions of low resolution approach those that are as good as the resolution allows. Since simulations are often run that depend on the accurate evolution of small wavelengths, this last point is important. We conclude that a higher order, shock capturing scheme such as PPM is essential for cosmological work and also that the modifications described here produce a robust, high resolution code.

The code has been written in FORTRAN 77 and runs at 1.3×10^4 zone-cycles per second on one processor of a Convex 3880 (1.7×10^4 zone-cycles per second without the N-body solver and Poisson solver). It has also been converted to CM FORTRAN, a data parallel language similar to FORTRAN 90 that is used on the massively parallel Connection Machine 5. It runs at 1×10^6 zone-cycles per second on 512 nodes (2×10^6 zone-cycles per second without the N-body solver and 4×10^6 without the Poisson solver).

Acknowledgements

We are grateful for support from NSF HPCC grant ASC93-181815. GLB and MLN were supported in part by NASA grant NAGW-3152. RC and JPO were supported in part by NASA grant NAGW-2448 and NSF

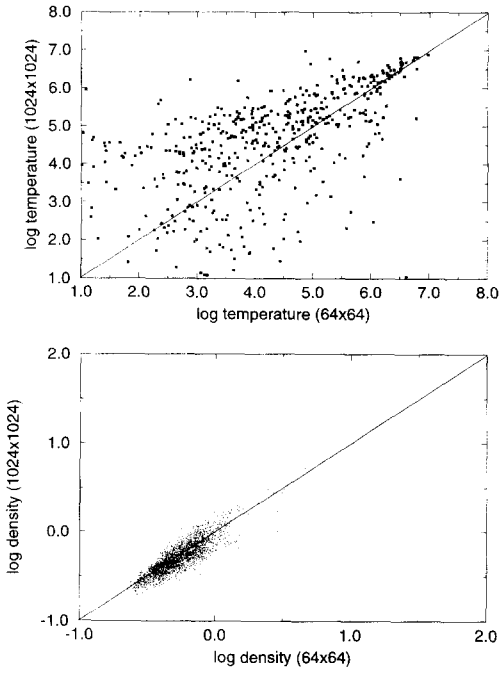

Fig. 12.

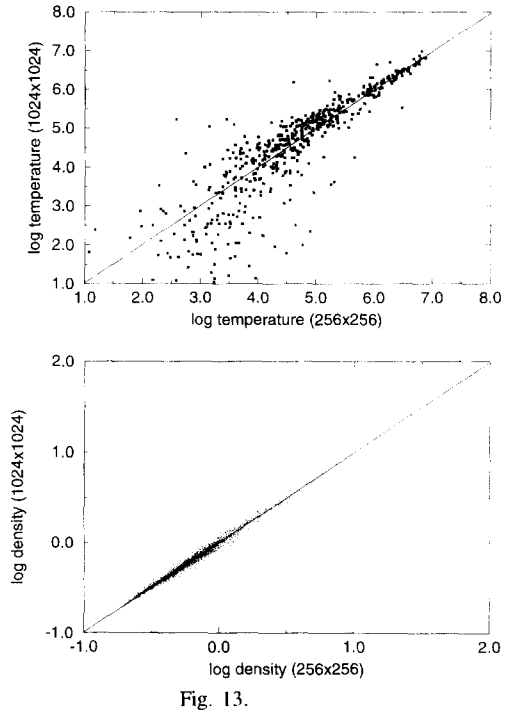

Fig. 13.

Fig. 12. Scatter plots of temperature (top) and density (bottom) for a two-dimensional CDM simulation computed with 64 × 64 zones compared on a cell-by-cell basis against a simulation computed with 1024 × 1024 cells and degraded to 64 × 64. Temperature is in degrees Kelvin, density in units of the present density required to close the universe.

Fig. 13. Similar plots as in the previous figure, except for a simulation computed with 256 × 256 zones.

grant AST91-08103. Development and testing of this code was done at the National Center for Supercomputing Applications using the Convex C3880, Cray YMP and Connection Machine 5 computer systems.

References

[1] R. Cen and J.P. Ostriker, Astrophys. J. 399 (1992) L113.
[2] R. Cen and J.P. Ostriker, Astrophys. J. 417 (1993) 415.
[3] N. Katz, L. Hernquist and D. Weinberg, Astrophys. J. 399 (1992) L109
[4] R.W. Hockney and J.W. Eastwood, Computer Simulation Using Particles (McGraw-Hill. New York, 1980).
[5] P. Colella and P.R. Woodward, J. Comput. Phys. 54 (1984) 174.
[6] G. Efstathiou, M. Davis, C.S. Frenk, and S.D.M. White, Astrophys. J. Suppl. Series 57 (1985) 241.
[7] M. Davis, G. Efstathiou, C.S. Frenk, and S.D.M. White, Astrophys. J. 292 (1985) 371.
[8] G. Strang, SIAM J. Num. Anal. 5 (1968) 506.
[9] L. Hernquist and N. Katz, Astrophys. J. Suppl. Series 70 (1989) 419.
[10] A. E. Evrard, Mon. Not. R. Astron. Soc. 235 (1988) 911.
[11] R. Cen Astrophys. J. Suppl. Series 78 (1992) 341.
[12] D. Ryu, J.P. Ostriker, H. Kang and R. Cen, Astrophys. J. 414 (1993) 1.
[13] P.J.E. Peebles, The Large-Scale structure of the Universe (Princeton University Press, Princeton, 1980).
[14] D. Layzer, Ann. Rev. Astron. Astrophys. 2 (1964) 341.
[15] W.M. Irvine, Ann. Phys. 32 (1965) 322
[16] P.R. Woodward, Astrophysical Radiation Hydrodynamics, eds. K.-H. Winkler and M.L. Norman (Reidel, Dordrecht, 1986).
[17] P.R. Woodward and P. Colella, J. Comput. Phys. 54 (1984) 115.

[18] E. Bertschinger, Astrophys. J. Suppl. 58 (1985) 39.
[19] C. Hunter, Astrophys. J. 136 (1962) 594.
[20] J.M. Stone and M.L. Norman, Astrophys. J. 80 (1992) 753.
[21] J.W. Eastwood and D.R.K. Brownrigg, J. Comput. Phys. 32 (1979) 24.
[22] Ya.B. Zel'dovich, Astron. Astrophys. 5 (1970) 84.
[23] W. Anninos and M.L. Norman, Astrophys. J., submitted.
[24] J.M. Bardeen, J.R. Bond, M. Kaiser and A.S. Szalay, Astrophys. J. 304 (1986) 15.
[25] H. Kang, J.P. Ostriker, R. Cen, D. Ryu, L. Hernquist, A.E. Evrard, G.L. Bryan and M.L. Norman, Astrophys. J., submitted (1994).